Chemical Science

ROYAL SOCIETY OF CHEMISTRY

EDGE ARTICLE

View Article Online
View Journal | View Issue

Open Access Article. Published on 14 September 2020. Downloaded on 10/24/2025 5:08:13 AM.
This article is licensed under a Creative Commons Attribution 3.0 Unported Licence.

Check for updates

Cite this: *Chem. Sci.*, 2020, **11**, 11195

All publication charges for this article have been paid for by the Royal Society of Chemistry

Revealing the relationship between photoelectrochemical performance and interface hole trapping in $CuBi_2O_4$ heterojunction photoelectrodes†

Angang Song,[ab] Igal Levine,[c] Roel van de Krol,[ab] Thomas Dittrich *[c] and Sean P. Berglund *[a]

p-Type $CuBi_2O_4$ is considered a promising metal oxide semiconductor for large-scale, economic solar water splitting due to the optimal band structure and low-cost fabrication. The main challenge in utilizing $CuBi_2O_4$ as a photoelectrode for water splitting, is that it must be protected from photocorrosion in aqueous solutions, an inherent problem for Cu-based metal oxide photoelectrodes. In this work, several buffer layers (CdS, $BiVO_4$, and Ga_2O_3) were tested between $CuBi_2O_4$ and conformal TiO_2 as the protection layer. RuO_x was used as the co-catalyst for hydrogen evolution. Factors that limit the photoelectrochemical performance of the $CuBi_2O_4/TiO_2/RuO_x$, $CuBi_2O_4/CdS/TiO_2/RuO_x$, $CuBi_2O_4/BiVO_4/TiO_2/RuO_x$ and $CuBi_2O_4/Ga_2O_3/TiO_2/RuO_x$ heterojunction photoelectrodes were revealed by comparing photocurrents, band offsets, and directed charge transfer measured by modulated surface photovoltage spectroscopy. For $CuBi_2O_4/Ga_2O_3/TiO_2/RuO_x$ photoelectrodes, barriers for charge transfer strongly limited the performance. In $CuBi_2O_4/CdS/TiO_2/RuO_x$, the absence of hole traps resulted in a relatively high photocurrent density and faradaic efficiency for hydrogen evolution despite the presence of pronounced deep defect states at the $CuBi_2O_4$/CdS interface. Hole trapping limited the performance moderately in $CuBi_2O_4/BiVO_4/TiO_2/RuO_x$ and strongly in $CuBi_2O_4/TiO_2/RuO_x$ photoelectrodes. For the first time, our results show that hole trapping is a key factor that must be addressed to optimize the performance of $CuBi_2O_4$-based heterojunction photoelectrodes.

Received 30th May 2020
Accepted 12th September 2020

DOI: 10.1039/d0sc03030a

rsc.li/chemical-science

Introduction

Copper bismuth oxide ($CuBi_2O_4$) is a promising photoabsorber for photoelectrochemical (PEC) water splitting due to its optimal optical bandgap (1.5–1.8 eV), positive photocurrent onset potential (more positive than 1 V *vs.* RHE), and Earth-abundant chemical composition.[1–4] However, several limitations in $CuBi_2O_4$ must be overcome to improve its performance as a photocathode for the hydrogen evolution reaction. Perhaps the greatest limitation of $CuBi_2O_4$ is its susceptibility to photocorrode under illumination in aqueous solutions, which is a common problem for Cu-based metal oxide photoelectrodes.[5–8] Surface modification *via* the formation of a heterojunction with a suitable buffer layer and/or an n-type protection layer could be highly effective at overcoming this limitation of $CuBi_2O_4$ based on previous reports on other Cu-based metal oxide photocathodes such as Cu_2O, CuO and $CuFeO_4$ as well as Si-based photoelectrodes.[9–13]

To be effective, a suitable buffer layer and/or protective layer must cover $CuBi_2O_4$ conformally without any pinholes and have energy band positions that match favorably to allow for efficient transport of charge carriers across the solid-state and semiconductor–electrolyte interfaces. TiO_2 deposited by atomic layer deposition (ALD) has been reported as an excellent protective layer for unstable photoelectrodes while simultaneously allowing for efficient electron transfer to the electrolyte under the PEC conditions for hydrogen evolution.[11,14–16] Studies have shown that TiO_2-protected Cu_2O-based photocathodes exhibit a relatively high photocurrent density and significantly enhanced stability when using various buffer layers between Cu_2O and TiO_2 such as ZnO and Al doped ZnO (AZO).[15,17,18] However, relatively poor photocurrent onset potentials (0.45–

[a]Institute for Solar Fuels, Helmholtz-Zentrum Berlin für Materialien und Energie GmbH, Hahn-Meitner-Platz 1, 14109 Berlin, Germany. E-mail: sean.berglund@gmail.com

[b]Institut für Chemie, Technische Universität Berlin, Straße des 17. Juni 124, 10623 Berlin, Germany

[c]Institute for Silicon Photovoltaics, Helmholtz-Zentrum Berlin für Materialien und Energie GmbH, Kekuléstr. 5, 12489 Berlin, Germany. E-mail: dittrich@helmholtz-berlin.de

† Electronic supplementary information (ESI) available. See DOI: 10.1039/d0sc03030a

Open Access Article. Published on 14 September 2020. Downloaded on 10/24/2025 5:08:13 AM.
This article is licensed under a Creative Commons Attribution 3.0 Unported Licence.

0.55 V *vs.* RHE) were obtained in this structure due to the small photovoltage produced by the heterojunctions. It has been shown that the use of ZnS as a buffer layer between Cu_2O and TiO_2 can increase the photovoltage at the multilayer/electrolyte junction thereby shifting the onset potential cathodically to 0.7 V *vs.* RHE.[19] The introduction of Ga_2O_3 as a buffer layer between Cu_2O and TiO_2 can improve the photovoltage even further (open-circuit voltage up to 1.2 V for Cu_2O solar cells[20] and photocurrent onset above 1.0 V *vs.* RHE for photocathodes).[21–23] In another work for CuO-based heterojunction photocathodes, ZnO showed rather poor performance as a buffer layer, in contrast to CdS.[24]

The band positions of the various layers within TiO_2-protected heterojunction photocathodes are crucial in determining the overall performance. The photovoltage of the device is ultimately limited by the difference in the Fermi level of the photoabsorber and the conduction band of either the buffer layer or the TiO_2 protective layer, depending on which has a lower conduction band.[5] Furthermore, numerous studies have emphasized the importance of band alignment between the photoabsorber and the buffer layer. In addition to band alignment, other key factors related to recombination and/or trapping at the layer interfaces can contribute to the overall performance. For example, it was recently shown by model calculations that Al-doped ZnO (AZO) buffer layers between Cu_2O and TiO_2 should enable a higher photovoltage than Ga_2O_3 buffer layers, but AZO may induce an interface recombination layer that hinders charge transfer and thus decreases the photovoltage.[9] Therefore, in addition to optimal band energy alignment, heterojunction interface layers must be high-quality and possess low interfacial trap densities to maximize device performance. Incidentally, compared to band positions, defect states and recombination sites at interfaces are often more difficult to characterize. Modulated surface photovoltage (SPV) spectroscopy can be used to provide information about electronic transitions from which photogeneration can take place and about the direction of charge separation even over very short distances and with very high sensitivity.[25,26]

In order to obtain information about dominant limiting factors in heterojunction photoelectrodes with $CuBi_2O_4$ as the absorber layer and ALD-deposited TiO_2 as the protective layer, we compared how different buffer layers (CdS, $BiVO_4$, and Ga_2O_3) affected the photocurrent density (with RuO_x as a co-catalyst layer for H^+ reduction reaction) as well as the behavior of modulated SPV spectra. Fig. 1 shows the layer stacking of the various heterojunction photoelectrodes that were tested in this work. The energy positions of the valence band edges in the separate layers were measured by photoelectron spectroscopy. Our results show that, in addition to suitable band alignment for charge transfer, preferential trapping of holes at $CuBi_2O_4/TiO_2$, $CuBi_2O_4/BiVO_4$ and $CuBi_2O_4/Ga_2O_3$ interfaces drastically limits the photocurrent of the corresponding PEC systems. In contrast, preferential trapping of electrons at the $CuBi_2O_4$/CdS interface limits the photocurrent to a much lesser extent despite the appearance of pronounced deep defect states.

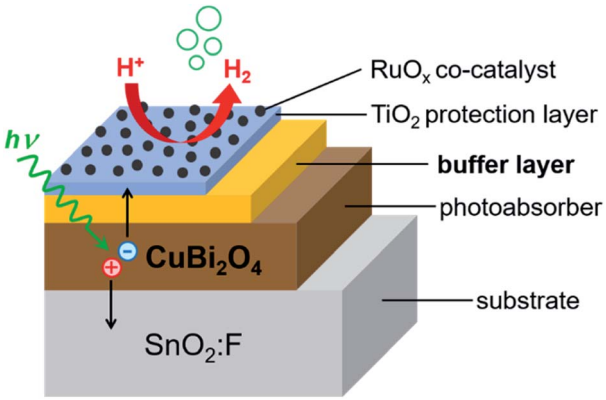

Fig. 1 Schematic of the layer stacking for the heterojunction photoelectrodes analyzed in this work. A TiO_2 protection layer was used in all cases, which was deposited either directly on the $CuBi_2O_4$ absorber, or on the Ga_2O_3, $BiVO_4$, or CdS buffer layer. RuO_x was used as a co-catalyst for the hydrogen evolution reaction. The substrate was SnO_2 : F, fluorine-doped tin oxide (FTO).

Results and discussion

Photoelectrochemical analysis

In this work we performed PEC measurements on bare $CuBi_2O_4$ photocathodes in addition to the $CuBi_2O_4/CdS/TiO_2/RuO_x$, $CuBi_2O_4/Ga_2O_3/TiO_2/RuO_x$, $CuBi_2O_4/BiVO_4/TiO_2/RuO_x$ and $CuBi_2O_4/TiO_2/RuO_x$ heterojunction photoelectrodes. They were measured under chopped AM 1.5 illumination in 0.3 M K_2SO_4 and 0.2 M phosphate buffer (pH 6.8) with Ar bubbling to purge dissolved oxygen from the electrolyte. As shown in Fig. S1a in the ESI,† the bare $CuBi_2O_4$ electrode exhibited a relatively large cathodic photocurrent density of -1 mA cm^{-2} at 0.4 V *vs.* RHE under visible light illumination for the chopped linear sweep voltammetry (LSV) measurement. However, the photocurrent density decayed rapidly, as shown in the constant potential measurement under illumination at 0.6 V *vs.* RHE (see Fig. S1b†). Based on previous reports this is attributed to the reduction of Cu^{2+} to Cu^{1+} and/or Cu in aqueous solution.[1,27–29] After 30 minutes the photocurrent density was only 6.4% of the initial value and by the end of the 5 hour measurement the illuminated area of the photoelectrode was transparent (see the inset of Fig. S1b†) presumably because the reduced copper dissolved into the electrolyte. Differential mass spectrometry (DEMS) measurements confirmed that the bare $CuBi_2O_4$ photocathodes did not produce a detectable amount of hydrogen (see Fig. S1c†).

The chopped LSV curves for the $CuBi_2O_4/CdS/TiO_2/RuO_x$, $CuBi_2O_4/Ga_2O_3/TiO_2/RuO_x$, $CuBi_2O_4/BiVO_4/TiO_2/RuO_x$ and $CuBi_2O_4/TiO_2/RuO_x$ heterojunction photoelectrodes are shown in Fig. 2a. Unlike the bare $CuBi_2O_4$ photocathode, the heterojunction photoelectrodes showed minimal dark currents at potentials more negative than 0.35 V *vs.* RHE, indicating that the ALD-deposited TiO_2 layer effectively inhibits the electrochemical corrosion of the underlying $CuBi_2O_4$. However, the photocurrent generated from the $CuBi_2O_4/TiO_2/RuO_x$ and $CuBi_2O_4/Ga_2O_3/TiO_2/RuO_x$ photocathodes (blue and black

Open Access Article. Published on 14 September 2020. Downloaded on 10/24/2025 5:08:13 AM.
This article is licensed under a Creative Commons Attribution 3.0 Unported Licence.

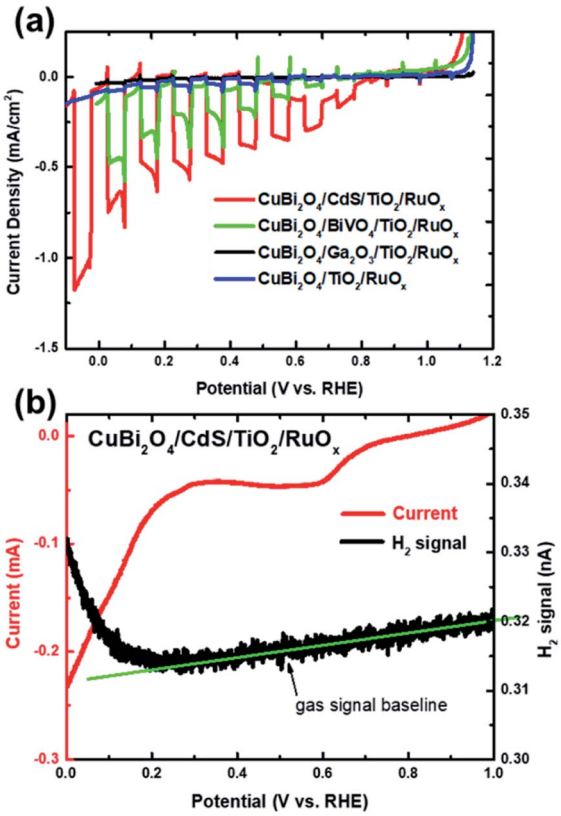

Fig. 2 (a) Chopped LSV scans for a $CuBi_2O_4/CdS/TiO_2/RuO_x$ (red), $CuBi_2O_4/BiVO_4/TiO_2/RuO_x$ (green), $CuBi_2O_4/Ga_2O_3/TiO_2/RuO_x$ (black) and $CuBi_2O_4/TiO_2/RuO_x$ photocathode (blue) under simulated AM1.5 illumination (these are representative measurements of at least 4 samples for each condition). (b) Differential electrochemical mass spectrometry (DEMS) LSV scans for a $CuBi_2O_4/CdS/TiO_2/RuO_x$ photocathode with illumination by a xenon lamp, showing current (red) and H_2 signal (black). Measurements were performed in three-electrode configuration in 0.3 M K_2SO_4 and 0.2 M phosphate buffer electrolyte (pH 6.8) with Ar bubbling.

lines) were very small (*ca.* −0.04 mA cm^{-2} and −0.01 mA cm^{-2} at 0 V *vs.* RHE, respectively). This indicates that the $CuBi_2O_4/TiO_2$ and the $CuBi_2O_4/Ga_2O_3$ or Ga_2O_3/TiO_2 interfaces in these samples do not effectively charge transport to the RuO_x co-catalyst layer and into the electrolyte. The $CuBi_2O_4/BiVO_4/TiO_2/RuO_x$ photoelectrode (green line) shows significantly higher photocurrent density (*ca.* −0.5 mA cm^{-2} at 0 V *vs.* RHE) while the $CuBi_2O_4/CdS/TiO_2/RuO_x$ photoelectrode (red line) shows by far the highest photoactivity with a plateau in photocurrent density at *ca.* −1 mA cm^2 at 0 V *vs.* RHE. It also has the most positive photocurrent onset at 0.8 V *vs.* RHE. For the $CuBi_2O_4/CdS/TiO_2/RuO_x$ photoelectrode the bump in the dark current around 0.5–0.6 V *vs.* RHE is likely due to the reduction of dissolved oxygen that could not be completely purged from the PEC cell by Ar bubbling,[5] or another reduction process on the electrode surface such as the pre-reduction of the RuO_x catalyst.[16] The DEMS measurement (Fig. 2b) shows that when the photocurrent increases cathodically at potentials negative of 0.3 V *vs.* RHE (red line) there is a simultaneous increase in H_2 signal (black line) confirming that the $CuBi_2O_4/CdS/TiO_2/RuO_x$ heterojunction photoelectrode can evolve hydrogen photoelectrochemically. The faradaic efficiency was estimated to be 92% based on calibration of the DEMS using a Pt metal electrode.

Note that the photocurrent density directly before the onset of dark current from electrochemical proton reduction (*ca.* −1 mA cm^2 at 0 V *vs.* RHE in Fig. 2a) is close to the maximum photocurrent density for bare $CuBi_2O_4$ before the onset of dark current from electrochemical corrosion (*ca.* −1 mA cm^{-2} at 0.4 V *vs.* RHE in Fig. S1a†). This implies that most of the electrons that are photogenerated in $CuBi_2O_4$, which previously participated in the corrosion reaction ($Cu^{2+} \rightarrow Cu^{1+}$ and/or Cu), are successfully injected into the CdS buffer and TiO_2 protection layers, and eventually into the electrolyte to drive the hydrogen evolution reaction.

In order to investigate the long-term stability of the $CuBi_2O_4/CdS/TiO_2/RuO_x$ photocathodes, the photocurrent density was measured at a constant potential of 0.0 V *vs.* RHE for 5 hours with intermittent chopping of the front illumination (see Fig. S2 in the ESI†). The measurement shows a decay in photocurrent which was more than 100 times slower than for the bare $CuBi_2O_4$ photocathode (Fig. S1b†). A significant part of the decay was attributed to deterioration of the RuO_x co-catalyst as demonstrated by partial restoration of the photocurrent after re-deposition of RuO_x after 3 hours. At the end of the 5 hour measurement, and after the single re-deposition of the RuO_x co-catalyst, 30% of the initial photocurrent density was preserved. Visually the illuminated area of the $CuBi_2O_4/CdS/TiO_2/RuO_x$ photoelectrode was almost indistinguishable from the non-illuminated area (see the inset of Fig. S2†). Under scanning electron microscope (SEM) there were no significant morphological differences between areas of the sample that were and were not PEC tested other than a slight smoothing of the electrode surface after PEC testing (see Fig. S3†). Therefore, the ALD-deposited TiO_2 layer effectively blocked the contact between $CuBi_2O_4$ and the aqueous electrolyte and hindered photo-corrosion. This was also the case for the other layer systems. For comparison, photos and SEM images of the $CuBi_2O_4/CdS/TiO_2$, $CuBi_2O_4/Ga_2O_3/TiO_2$ and $CuBi_2O_4/BiVO_4/TiO_2$ photoelectrodes are shown in Fig. S4–S6,† respectively.

Band alignment

In order to estimate the band positions of the different materials in the heterojunction photoelectrodes, the energy band offsets were measured through a combination of X-ray photoelectron spectroscopy (XPS), ultraviolet photoelectron spectroscopy (UPS), UV-visible spectrophotometry, and Mott–Schottky analysis (including work from previous studies). Fig. S7a† shows the XPS spectrum for Cu at the surface of bare $CuBi_2O_4$. There are two main peaks at 933.8 and 953.6 eV corresponding to the Cu $2p_{3/2}$ and $2p_{1/2}$ levels, both of which were attributed to the presence of the Cu^{2+} state on the surface.[30] The binding energies of Cd 3d, Ga 3d, V 2p and Ti 2p core levels of CdS, Ga_2O_3, $BiVO_4$ and TiO_2 are measured to be 406.3, 21.2, 516.7 and 459.3 eV, respectively (see Fig. S7b–e†). Fig. S8† shows the XPS survey results for the stack samples of the $CuBi_2O_4/CdS/$

Open Access Article. Published on 14 September 2020. Downloaded on 10/24/2025 5:08:13 AM. This article is licensed under a Creative Commons Attribution 3.0 Unported Licence.

TiO_2, $CuBi_2O_4/Ga_2O_3/TiO_2$, $CuBi_2O_4/BiVO_4/TiO_2$ and $CuBi_2O_4/TiO_2$. The presence of strong Ti peaks and the absence of Cu, Cd, Ga and V peaks in the survey spectra indicates that the ALD-deposited TiO_2 layer fully covers the buffer layers.

For the band positions of bare $CuBi_2O_4$, we used our previously reported values from Mott–Schottky analysis and UPS measurements, to estimate a conduction band (E_C) of −0.3 V *vs.* RHE and a valence band (E_V) of 1.2 V *vs.* RHE.[4,5,31] The flat-band potential (φ_{fb}) of our spray-deposited $BiVO_4$ films is 0.37 V *vs.* RHE,[5,32] which can then be used to estimate the Fermi level (E_F) while taking into account the potential drop across the Helmholtz layer.[5,33] Fig. S9a–c† show the UPS spectra of CdS, Ga_2O_3 and TiO_2 thin films on FTO substrate measured with a 2 V bias. The work function (Φ), defined as the difference between the vacuum energy level and Fermi level (E_F), can be derived from the low kinetic energy cut-off in the secondary emission feature. The photon energy of the UV source (He I discharge) was 21.21 eV. Given that the Fermi level at the surface of these overlayers is considered independently of the spectrometer, the work function is determined to be 21.21 − 2 − secondary emission cut-off (SEC). The work function of CdS, Ga_2O_3 and TiO_2 thin films are calculated to be 4.12, 3.63 and 4.57 eV, respectively. Using 4.5 eV *vs.* vacuum as the reference value for the electrochemical proton reduction (0.0 V *vs.* RHE) we can estimate the Fermi energies of the CdS, Ga_2O_3 and TiO_2 layers at approximately −0.38, −0.87 and 0.07 V *vs.* RHE, respectively. These values are in agreement with the literature.[34–36]

The valence band positions with respect to the position of the Fermi level, $E_F - E_V$, were determined by linear extrapolation of the UPS spectrum at the low binding energy side to the binding energy axis (see Fig. S10†). $E_F - E_V$ for CdS, $BiVO_4$, Ga_2O_3 and TiO_2 thin films are calculated to be 2.5, 2.4, 4.6, and 3.3 eV, respectively, which is consistent with previously reported values.[37,38] Since CdS has a bandgap of 2.4–2.5 eV this would place the conduction band very close to the Fermi level at −0.38 V *vs.* RHE, which is within the wide range of previously reported E_C values for CdS.[5,39,40] The experimentally determined band energy values for all samples are summarized in Table S1 in the ESI† along with values from the literature.

Using the values given in Table S1,† the energies of conduction and valence bands were obtained and illustrated in Fig. 3 for the individual layers in the $CuBi_2O_4/CdS/TiO_2$, $CuBi_2O_4/Ga_2O_3/TiO_2$ and $CuBi_2O_4/BiVO_4/TiO_2$ heterojunction photoelectrodes in relation to the electrochemical redox potentials for proton reduction (H^+/H_2) and water oxidation (H^+, O_2/H_2O) at 0.0 and 1.23 V *vs.* RHE, respectively. Since the conduction band of $CuBi_2O_4$ is at −0.3 V *vs.* RHE and the Fermi level of TiO_2 is at approximately 0.0 V *vs.* RHE, all of the heterojunctions shown in Fig. 3 should be thermodynamically capable of reducing H^+ as long as photogenerated electrons can be transported to the TiO_2 surface. However, there are differences in the conduction band offsets between $CuBi_2O_4$ and each buffer layer ($\Delta E_{C,1}$) and between TiO_2 and each buffer layer ($\Delta E_{C,2}$). For a wide range of heterojunctions, including CuO/TiO_2 junctions, it has been shown that a high conduction band offset can promote high interface recombination and therefore inhibit charge transport.[41] Better band alignment of the $CuBi_2O_4$/buffer layer provides a larger driving force for charge transport in $CuBi_2O_4$, results in a smaller concentration of holes near the interface and reduces the interfacial recombination. For all of the systems shown in Fig. 3, $\Delta E_{C,1}$ is by far the smallest between $CuBi_2O_4$ and CdS (less than 0.2 eV) while it is approximately 0.57 eV between $CuBi_2O_4$ and $BiVO_4$ and −0.67 eV between $CuBi_2O_4$ and Ga_2O_3 assuming that E_C is approximately 0.1 eV above E_F in the buffer layers. The significantly higher conduction band of Ga_2O_3 compared to $CuBi_2O_4$ creates an energy barrier, thus significantly limiting the charge separation efficiency and the injection of the photogenerated electrons to the TiO_2, which increases the recombination rate of photogenerated electrons and holes at the $CuBi_2O_4/Ga_2O_3/TiO_2$ interfaces, especially if they contain defect states. This alone is enough to explain the poor performance of the $CuBi_2O_4/Ga_2O_3/TiO_2/RuO_x$ photoelectrode compared to the others. For all of the heterojunctions shown in Fig. 3, $\Delta E_{C,2}$ is also smallest with CdS as the buffer layer. For the $CuBi_2O_4/BiVO_4/TiO_2$ system, transport of photogenerated electrons from $CuBi_2O_4$ to $BiVO_4$ is thermodynamically favorable, but the $\Delta E_{C,2}$ value of −0.27 eV may hinder transport of these electrons into TiO_2. Overall, the relatively small conduction band offsets between $CuBi_2O_4$, CdS, and TiO_2 makes the $CuBi_2O_4/CdS/TiO_2$ heterojunction photoelectrode more favorable for obtaining a high photovoltage and transporting charges compared to the $CuBi_2O_4/Ga_2O_3/TiO_2/RuO_x$ and $CuBi_2O_4/BiVO_4/TiO_2/RuO_x$ photoelectrodes.

Based on these energy band diagrams the $CuBi_2O_4/TiO_2/RuO_x$ photoelectrode is also expected to contain a relatively small band offset of approximately 0.3 eV between $CuBi_2O_4$ and TiO_2. Therefore, assuming negligible formation of interface dipoles, the performance of the $CuBi_2O_4/TiO_2/RuO_x$ photoelectrode is expected to be comparable to $CuBi_2O_4/CdS/TiO_2/RuO_x$ and higher than the $CuBi_2O_4/BiVO_4/TiO_2/RuO_x$ heterojunction system. As shown in Fig. 2a, this is clearly not the case, suggesting that additional factors aside the band offsets probably play an important role in the heterojunction systems. One of these factors, common in the case of heterojunctions, is the formation of intermixed interface layers, which may serve as hole or electron traps and hinder charge transfer.

Surface photovoltage analysis

To understand the relation between the charge transfer kinetics in the various heterojunctions and their PEC performance, modulated surface photovoltage (SPV) spectroscopy in the fixed capacitor arrangement was utilized.[26] Aside from its very high sensitivity, modulated SPV spectroscopy can provide information about fast and slow (or retarded) processes in relation to the modulation period. Modulated SPV spectra are measured with double-phase lock-in amplifiers. The in-phase (x) and phase-shifted by 90° (y) signals are related to the fast and slow responses, respectively. In general, the response times of the SPV are much shorter (or longer) than the modulation period after switching on and off illumination if y (or x) are equal to 0. Furthermore, positive (or negative) x-signals are related to preferential separation of photogenerated electrons towards the bulk (or surface) of the absorber. The sign of the y-signal in

Open Access Article. Published on 14 September 2020. Downloaded on 10/24/2025 5:08:13 AM.
This article is licensed under a Creative Commons Attribution 3.0 Unported Licence.

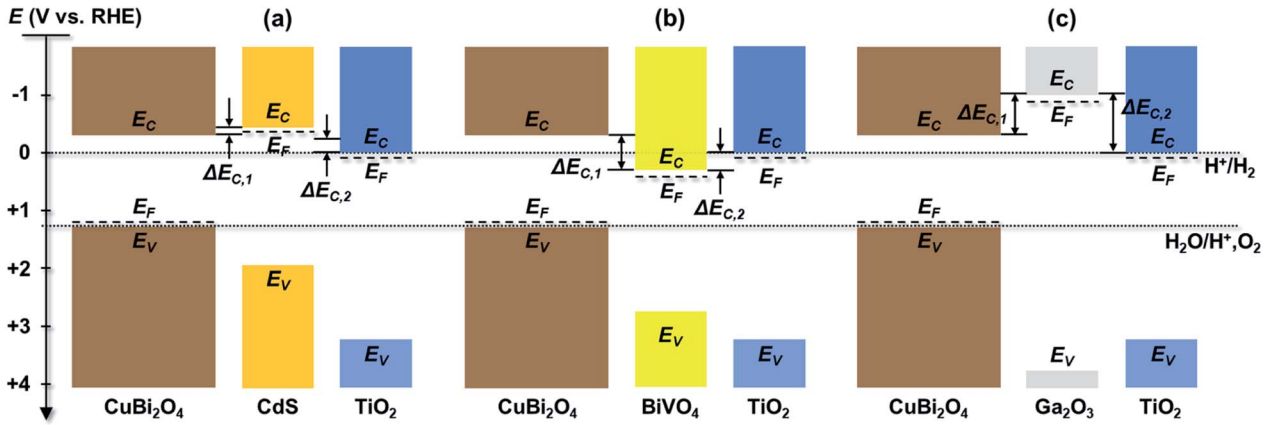

Fig. 3 Estimated band diagrams for systems containing (a) $CuBi_2O_4/CdS/TiO_2$, (b) $CuBi_2O_4/BiVO_4/TiO_2$ and (c) $CuBi_2O_4/Ga_2O_3/TiO_2$ in relation to electrochemical redox potentials for proton reduction (H^+/H_2) and water oxidation (H^+, O_2/H_2O). E_F is the Fermi level, E_C is the conduction band, E_V is the valence band, and $\Delta E_{C,1}$ and $\Delta E_{C,2}$ are the conduction band offsets.

relation to the sign of the *x*-signal gives information about the preferential direction of trapped charge carriers. If the *x*- and *y*-signals are of opposite sign, the direction of separated trapped charge carriers is similar to that of fast charge separation and relaxation. In contrast, if the *x*- and *y*-signals have the same sign, the directions of separated charge carriers are opposite for the dominating fast and slow processes (see Fig. S11† for a schematic illustration, and for more detailed explanations also paragraph 2.3.4. in ref. 26 or the ESI in ref. 42).

To start, in order to compare between the different samples in terms of their general SPV response (not separated to slow and fast components), the *x*- and *y*-signals can be converted into amplitudes. The amplitude is defined as the square root of the sum of the squared *x*- and *y*-signals. The amplitude spectra of the $CuBi_2O_4/CdS/TiO_2$, $CuBi_2O_4/BiVO_4/TiO_2$, $CuBi_2O_4/TiO_2$ and $CuBi_2O_4/Ga_2O_3/TiO_2$ systems are presented on a semi-log scale in Fig. 4. The extracted band gap of $CuBi_2O_4$, which is determined close to where the SPV deviates from exponential dependance, amounts to 1.55–1.6 eV, in agreement with our previous report.[5] When comparing the maximum measured SPV amplitudes, we find that there is no direct correlation between the maximum SPV signal and the PEC performance, *i.e.* for the $CuBi_2O_4/TiO_2$ sample, the maximum SPV amplitude is the highest, however for this sample very low photocurrent values were obtained compared to the samples containing CdS or $BiVO_4$ buffer layers (see Fig. 2a). Analysis of the amplitude signals below the bandgap can yield valuable information regarding tail states and other defect states in the bulk of the absorber as well as in the interfaces with the different protection layers. If assuming that charge separation is caused only by directed transport of mobile charge carriers in delocalized states, and the SPV measurements are performed in the low-signal case and under homogeneous absorption within the charge separation and/or diffusion lengths, and the *x*- and *y*-signals do not change their signs within the corresponding spectral range, an exponential increase of the amplitude near the band gap or the first derivative of a logistic growth function are directly related to the exponential distribution of states near the valence (or conduction) band edge or to the distribution of deep defect states, respectively, from which photogeneration into delocalized states takes place.

Thus, under the above assumptions, we find the following fitting functions were needed to obtain a good fit, depending on the sample:

$$R = A_1 \exp\left(\frac{E_{ph} - 1.6\ \text{eV}}{E_{t,1}}\right) \quad (1)$$

$$R = A_1 \exp\left(\frac{E_{ph} - 1.6\ \text{eV}}{E_{t,1}}\right) + A_2 \exp\left(\frac{E_{ph} - 1.6\ \text{eV}}{E_{t,2}}\right) \quad (2)$$

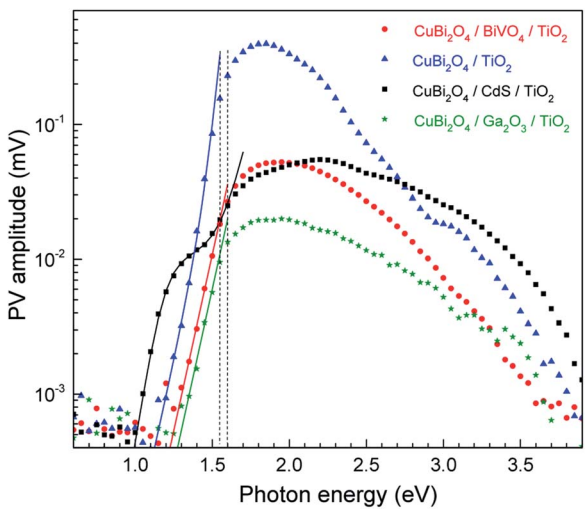

Fig. 4 Amplitude spectra of $CuBi_2O_4/CdS/TiO_2$, $CuBi_2O_4/BiVO_4/TiO_2$, $CuBi_2O_4/TiO_2$ and $CuBi_2O_4/Ga_2O_3/TiO_2$ (black squares, red circles, blue triangles and green stars, respectively). The solid green and red, blue, and black lines are fits below the band gap with one exponential term, the sum of two exponential terms, and the sum of a logarithmic growth and an exponential function for $CuBi_2O_4/Ga_2O_3/TiO_2$ and $CuBi_2O_4/BiVO_4/TiO_2$, $CuBi_2O_4/TiO_2$, and $CuBi_2O_4/CdS/TiO_2$, respectively. The two vertical dashed lines mark the approximate band gap range of $CuBi_2O_4$.

Open Access Article. Published on 14 September 2020. Downloaded on 10/24/2025 5:08:13 AM.
This article is licensed under a Creative Commons Attribution 3.0 Unported Licence.

$$R = \frac{A_d}{1 + \exp\left(\frac{E_{ph} - E_d}{E_{t,d}}\right)} + A_1 \exp\left(\frac{E_{ph} - 1.6\ \text{eV}}{E_{t,1}}\right) \quad (3)$$

For the $CuBi_2O_4/BiVO_4/TiO_2$ and $CuBi_2O_4/Ga_2O_3/TiO_2$ samples, a single exponential term (eqn (1)) was sufficient. For the $CuBi_2O_4/TiO_2$, a sum of two exponential terms was required (eqn (2)), and for the $CuBi_2O_4/CdS/TiO_2$ a sum of a logarithmic growth and an exponential function was required (eqn (3)). An identical band gap of 1.6 eV was used for all fits of the increasing part of the amplitude spectra. The main, common exponentials (eqn (1)) were characterized by the same tail energy ($E_{t,1}$) equal to 83 meV in all equations (we note that E_t is related, yet not equal to the so-called Urbach tail which is experimentally obtained from optical absorption). This gives evidence that $E_{t,1}$ is related to disorder-induced defect states near the band gap of the bulk of $CuBi_2O_4$ and that this disorder was not affected by the deposition of the different protection layers on top. Furthermore, the values of A_1 amounted to 20, 36, 130 and 15.5 μV for $CuBi_2O_4/Ga_2O_3/TiO_2$, $CuBi_2O_4/BiVO_4/TiO_2$, $CuBi_2O_4/TiO_2$ and $CuBi_2O_4/CdS/TiO_2$, respectively. Therefore, the strongest charge separation from defect states near the band gap of $CuBi_2O_4$ appeared in $CuBi_2O_4/TiO_2$.

The values of $E_{t,2}$ and A_2 were 35 meV and 600 μV, respectively. The fact that a second exponential term was required for fitting the increase of the SPV amplitude below the band gap of $CuBi_2O_4$ in $CuBi_2O_4/TiO_2$ gives evidence for the formation of an interface region with efficient absorption and modulated charge separation at reduced disorder near the band gap of $CuBi_2O_4$.

The logarithmic growth function in eqn (3) is related to the excitation and separation of mobile charge carriers due to absorption in relatively deep defect states (where E_d is denotes the maximum DOS of the defect distribution within the bandgap). The obtained E_d value amounts to 1.19 eV, about 400 meV within the bandgap of the $CuBi_2O_4$, in agreement with the deep defects observed in our previous work for this type of junction.[5] These deep defect states were specific for the $CuBi_2O_4/CdS$ interface since the defect related feature appeared only in the spectrum of $CuBi_2O_4/CdS/TiO_2$. It can therefore be concluded that partial inter-diffusion took place at the $CuBi_2O_4/CdS$ interface leading to the formation of deep interfacial states. In spite of these additional deep defect states that were found only in the $CuBi_2O_4/CdS/TiO_2$ sample, this sample had the highest PEC performance. Thus, in order to a gain deeper understanding of how the modulated charge separation and recombination processes affect and correlate to the actual PEC performance, it is essential to understand exactly which type of free and/or trapped charge carriers are accumulated at the different interfaces, by performing a detailed analysis of the individual x and y components of the SPV signals, as shown next.

Fig. 5 shows the modulated SPV spectra of the in-phase and phase-shifted by 90° signals for the $CuBi_2O_4/CdS/TiO_2$, $CuBi_2O_4/BiVO_4/TiO_2$, $CuBi_2O_4/TiO_2$ and $CuBi_2O_4/Ga_2O_3/TiO_2$, samples. Starting with the in-phase signals, that give indication into which type of free charge carriers accumulate closer to the sample's surface, it is found that in the absorption range of $CuBi_2O_4$, the signs of the in-phase signals where negative for $CuBi_2O_4/CdS/TiO_2$, $CuBi_2O_4/BiVO_4/TiO_2$, $CuBi_2O_4/TiO_2$ and bare $CuBi_2O_4$ with an uncontrolled surface. This finding gives evidence to separation of electrons towards the surface (as expected for a p-type absorber with an electron-selective contact or a p-type semiconductor with a depletion region near the surface), which is favorable for a photoreduction reaction such as proton reduction to take place at the surface. Incidentally, the signals of the bare $CuBi_2O_4$ layer with an uncontrolled surface were extremely low (only on the order of a μV) in comparison to the $CuBi_2O_4/CdS/TiO_2$, $CuBi_2O_4/BiVO_4/TiO_2$, and $CuBi_2O_4/TiO_2$ samples. This suggests that without an appropriate charge extraction layer, the surface of the $CuBi_2O_4$ is not passivated, and/or the charge separation efficiency within the $CuBi_2O_4$ depletion region is rather low. In contrast, for the $CuBi_2O_4/Ga_2O_3/TiO_2$ sample, the sign of the in-phase signals was positive and only on the order of several μV. The positive sign of the in-phase signals indicates separation of holes towards the surface, however due to the very low signal, the charge separation efficiency in this case is quite low (as shown schematically in Fig. 7d), explaining the poor PEC performance of the $CuBi_2O_4/Ga_2O_3/TiO_2/RuO_x$ heterojunction as a photocathode (Fig. 2a). This observed behavior is probably due to the unfavorable band alignment already discussed and shown in Fig. 3c.

With regards to the phase-shifted by 90° signals, positive phase-shifted by 90° signals were found for $CuBi_2O_4/CdS/TiO_2$ and $CuBi_2O_4/Ga_2O_3/TiO_2$, suggesting that for these two samples, electrons that were separated towards the external surface were trapped in the range of the $CuBi_2O_4/CdS$ or the $CuBi_2O_4/Ga_2O_3$ interfaces. The electron traps in the $CuBi_2O_4/CdS$ interface can probably be attributed to the deep defect states seen in the amplitude spectrum of the $CuBi_2O_4/CdS/TiO_2$ sample in the energy region of 1–1.5 eV. In contrast, the signs of the phase-shifted by 90° signals were negative for $CuBi_2O_4/BiVO_4/TiO_2$ and $CuBi_2O_4/TiO_2$, *i.e.* holes were separated towards the external surface and trapped. This finding suggests that for these two heterojunction types, predominant trap states for holes were formed at $CuBi_2O_4/BiVO_4$ and $CuBi_2O_4/TiO_2$ interfaces, as shown schematically in Fig. 5b and c. Such an accumulation of trapped holes at the interface with $CuBi_2O_4$, compared to trapped electrons in the case of $CuBi_2O_4/CdS$, is much more detrimental for the PEC performance since it will lead to an increase in the total number of photogenerated electrons that will (non-radiatively) recombine. This explains the lower observed photocurrents for $CuBi_2O_4/TiO_2$ heterojunction in Fig. 2a compared to $CuBi_2O_4/CdS/TiO_2$.

Although in both $CuBi_2O_4/BiVO_4/TiO_2$ and $CuBi_2O_4/TiO_2$ a combination of negative in-phase and phase-shifted by 90° signals was observed, the PEC performance of the $CuBi_2O_4/TiO_2$ sample was extremely poor compared to the sample with the $BiVO_4$ buffer layer, which requires explanation. This behavior can be attributed to an additional, pronounced difference that is observed with and without the $BiVO_4$ buffer layer: for the $CuBi_2O_4/TiO_2$ sample, in the region between 2.5–3.5 eV, the phase-shifted by 90° signal becomes larger than the in-phase

Open Access Article. Published on 14 September 2020. Downloaded on 10/24/2025 5:08:13 AM.
This article is licensed under a Creative Commons Attribution 3.0 Unported Licence.

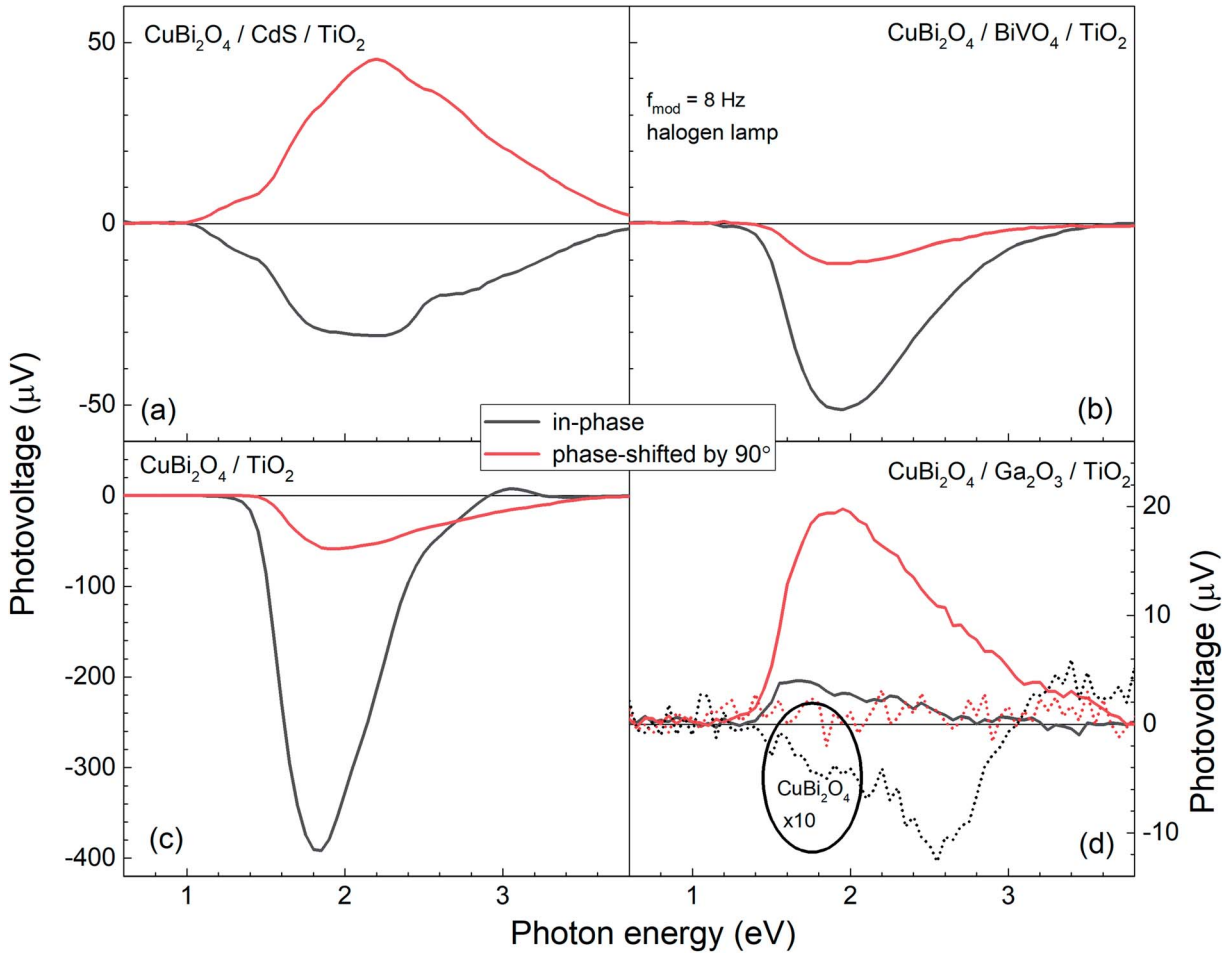

Fig. 5 Modulated SPV spectra of the in-phase and phase-shifted by 90° signals (black and red solid lines, respectively) for the $CuBi_2O_4/CdS/TiO_2$, $CuBi_2O_4/BiVO_4/TiO_2$, $CuBi_2O_4/TiO_2$ and $CuBi_2O_4/Ga_2O_3/TiO_2$, samples ((a)–(d), respectively). For comparison, the thin dashed black and red lines in (d) represent the measured in-phase and phase-shifted by 90° signals for a bare $CuBi_2O_4$ layer with uncontrolled surface.

signal, and the in-phase signal changes sign. Such pronounced qualitative differences can be analyzed quantitively by considering the so-called phase angle of the signal. The in-phase (x) and quadrature (y) components of the signal can be converted into the phase angle, which is defined as the arctan of the ratio between the y- and x-signals. Since the behavior of the x- and y-signals depends sensitively on transport and charge transfer processes, changes in the phase angle can provide information about changes in dominating processes in modulated charge separation. Spectra of the phase angles of $CuBi_2O_4/CdS/TiO_2$, $CuBi_2O_4/Ga_2O_3/TiO_2$, $CuBi_2O_4/BiVO_4/TiO_2$ and $CuBi_2O_4/TiO_2$ are given in Fig. 6.

For $CuBi_2O_4/CdS/TiO_2$, the phase angles changed from about 140° at 1.4 eV to 119° at 2.6 eV and to 124° at photon energies above 2.85 eV. Between 2.2 and 2.6 eV, the phase angle peaked slightly from 124° to 125° at 2.4 eV (band gap of CdS), decreased to the minimum of 119° at 2.6 eV, and then increased to its saturation value after that. Therefore, since those changes were small, absorption of light by defect states near the band gap of CdS and fundamental absorption in CdS led only to little modification in trapping.

For $CuBi_2O_4/Ga_2O_3/TiO_2$ and $CuBi_2O_4/BiVO_4/TiO_2$, the phase angles changed from about 75° to 86° and from about 189° to 196°, respectively. No well-defined signatures could be found within those weak changes. Therefore, deposition of Ga_2O_3 or $BiVO_4$ onto $CuBi_2O_4$ does not result in the formation of additional transitions that influence the trapping dynamics.

In contrast, drastic changes were observed in the spectrum of the phase angles for $CuBi_2O_4/TiO_2$. At photon energies between 1.45 and 2.15 eV, the phase angle increased from about 182° to 192°. The fact that the phase angles were so close to 180° means that the forward and backward electron transfer was the fastest at the $CuBi_2O_4/TiO_2$ interface. Between 2.15 and 2.7 eV, the phase angle increased strongly to 224° which means that the electron transfer became very slow in relation to the modulation period, *i.e.* strong electron trapping set in. The very strong change of the phase angles up to values exceeding 270° (296° at 3.05–3.10 eV) shows that a large change in the modulated charge separation occurs at these photon energies. Specifically, a phase angle around 270° indicates that the photo-generated holes move towards the external surface and/or that the photo-generated electrons move towards the $CuBi_2O_4/TiO_2$

Open Access Article. Published on 14 September 2020. Downloaded on 10/24/2025 5:08:13 AM.
This article is licensed under a Creative Commons Attribution 3.0 Unported Licence.

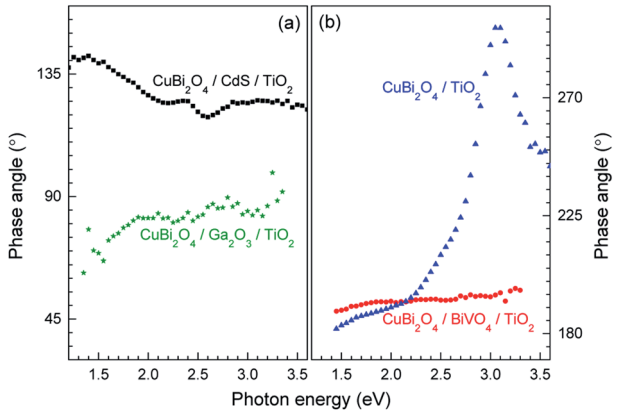

Fig. 6 Spectra of the phase angles of $CuBi_2O_4/CdS/TiO_2$ and $CuBi_2O_4/Ga_2O_3/TiO_2$ ((a), black squares and green stars, respectively) and of $CuBi_2O_4/BiVO_4/TiO_2$ and $CuBi_2O_4/TiO_2$ ((b), red circles and blue triangles, respectively).

interface. This explains the very poor performance of the $CuBi_2O_4/TiO_2$ photocathode sample without a buffer layer. At photon energies 3.1 eV, the phase angle changed towards lower values (244° at 3.6 eV) giving evidence for an increased influence of the separation of electrons photo-generated in TiO_2 towards the external surface. The very strong change of the phase angles for $CuBi_2O_4/TiO_2$ can only be interpreted by the formation of defect states within the band gap of TiO_2 near the $CuBi_2O_4/TiO_2$ interface, probably caused by inter-diffusion and/or partial reduction of TiO_2 by transferred and trapped holes. This notable difference in the dynamics and distribution of the charge carriers with and without the $BiVO_4$ buffer layer, illustrated in Fig. 7b and c, demonstrates the need to prevent direct contact between the $CuBi_2O_4$ and the TiO_2.

Based on the analysis of the SPV results and the correlation found with the PEC performance of the different heterojunctions, a schematic model illustrating the distribution of charge carriers in the different heterojunctions upon illumination with white light is shown in Fig. 7. The $CuBi_2O_4/CdS/TiO_2$ sample (Fig. 7a) shows the highest PEC performance, which we attribute to the uniform separation of free and trapped electrons toward the TiO_2 surface. When the CdS layer is replaced with $BiVO_4$ (Fig. 7b), interfacial hole traps are formed at the $CuBi_2O_4/BiVO_4$ interface, enhancing non-radiative recombination of electron–hole pairs and resulting in lower photocurrents. In the case of direct contact between the $CuBi_2O_4$ and TiO_2 (Fig. 7c), large defect-related SPV signals are observed, and a large majority of the photogenerated electrons and holes are trapped at the $CuBi_2O_4/TiO_2$ interface, resulting in poor PEC performance. For the case of $CuBi_2O_4/Ga_2O_3/TiO_2$ (Fig. 7d), the charge separation efficiency is quite low compared to the other heterojunctions, probably due to the large energetic barriers due to the higher conduction band of Ga_2O_3 shown in Fig. 3. The charge separation direction is not favorable for photocathodic reactions, explaining the very poor PEC performance observed. Overall, based on the modulated SPV results, it can be concluded that one of the most notable differences

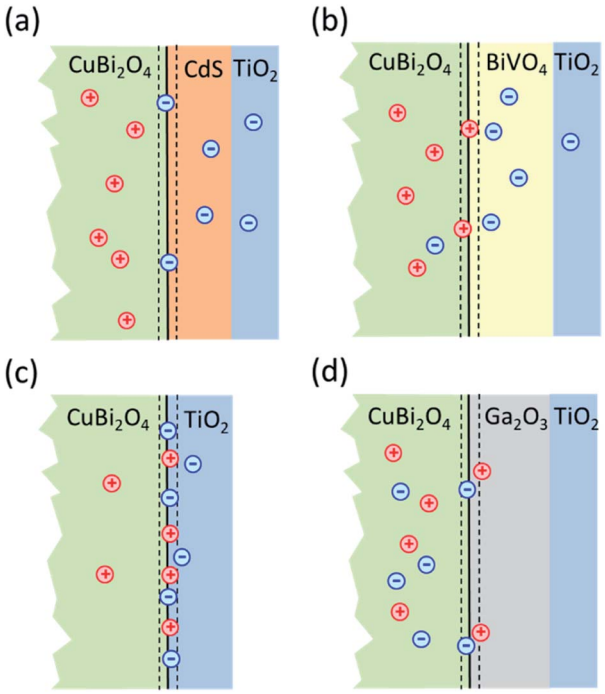

Fig. 7 Schematic model illustrating the distribution of charge carriers in the different heterojunctions upon illumination with white light: (a) $CuBi_2O_4/CdS/TiO_2$; (b) $CuBi_2O_4/BiVO_4/TiO_2$; (c) $CuBi_2O_4/TiO_2$ and (d) $CuBi_2O_4/Ga_2O_3/TiO_2$.

between the different heterojunctions is the lack of trapped holes in the heterojunction containing the CdS buffer layer. Hence, we conclude that trapped holes at the interface with the $CuBi_2O_4$ are the main cause for interfacial recombination and poor photocurrents.

Conclusions

In this work, we showed that photocurrents generated from bare, unprotected $CuBi_2O_4$ photocathodes were mainly due to photo-corrosion of $CuBi_2O_4$ and not from H_2 production, as claimed by many reports on Cu-based photocathodes. We investigated the influence of different buffer layers between the $CuBi_2O_4$ absorber and an n-type TiO_2 film that serves as a protection layer. We found that a CdS buffer layer in combination with the ALD-deposited TiO_2 protection layer and RuO_x co-catalyst layer yielded a stable photoelectrode with the highest photocurrent density and faradaic efficiency for the hydrogen evolution reaction. In contrast, neither high photocurrent nor efficient hydrogen evolution was obtained for $CuBi_2O_4/Ga_2O_3/TiO_2$, $CuBi_2O_4/BiVO_4/TiO_2$ and $CuBi_2O_4/TiO_2$ heterojunctions. However, band alignment considerations alone cannot explain the observed trends in photoelectrochemical performance. Therefore, modulated surface photovoltage measurements were used to investigate the mechanism governing the charge transport in these heterojunctions. The modulated SPV results strongly correlated with the observed trend of the photoelectrochemical performance and revealed the formation of different interfacial states, depending on the $CuBi_2O_4$/buffer

Open Access Article. Published on 14 September 2020. Downloaded on 10/24/2025 5:08:13 AM.
This article is licensed under a Creative Commons Attribution 3.0 Unported Licence.

layer junction. Most importantly, it revealed which type of charge carrier was trapped at the interface with the $CuBi_2O_4$ suggesting that trapping of holes near the interface strongly limits the photo-electrochemical performance of the heterojunctions.

Author contributions

The manuscript was written through contributions of all authors. All authors have given approval to the final version of the manuscript.

Conflicts of interest

There are no conflicts to declare.

Acknowledgements

Angang Song thanks the China Scholarship Council (file no. 201607040078) for financial support. We thank Christian Höhn for assistance with XPS and UPS measurements. We thank Lars Steinkopf for preparing CdS buffer layer and Matthias J. Müller for depositing the TiO_2 protection layer by ALD.

Notes and references

1 S. P. Berglund, F. F. Abdi, P. Bogdanoff, A. Chemseddine, D. Friedrich and R. van de Krol, *Chem. Mater.*, 2016, **28**, 4231–4242.
2 D. Kang, J. C. Hill, Y. Park and K.-S. Choi, *Chem. Mater.*, 2016, **28**, 4331–4340.
3 R. Patil, S. Kelkar, R. Naphade and S. Ogale, *J. Mater. Chem. A*, 2014, **2**, 3661–3668.
4 A. Song, P. Plate, A. Chemseddine, F. Wang, F. F. Abdi, M. Wollgarten, R. van de Krol and S. P. Berglund, *J. Mater. Chem. A*, 2019, **7**, 9183–9194.
5 A. Song, P. Bogdanoff, A. Esau, I. Y. Ahmet, I. Levine, T. Dittrich, T. Unold, R. van de Krol and S. P. Berglund, *ACS Appl. Mater. Interfaces*, 2020, **12**, 13959–13970.
6 H. Gerischer, *J. Electroanal. Chem. Interfacial Electrochem.*, 1977, **82**, 133–143.
7 S. Chen and L.-W. Wang, *Chem. Mater.*, 2012, **24**, 3659–3666.
8 Y. Xu, J. Jian, F. Li, W. Liu, L. Jia and H. Wang, *J. Mater. Chem. A*, 2019, **7**, 21997–22004.
9 P. Cendula, M. T. Mayer, J. Luo and M. Grätzel, *Sustainable Energy Fuels*, 2019, **3**, 2633–2641.
10 Y. W. Chen, J. D. Prange, S. Dühnen, Y. Park, M. Gunji, C. E. D. Chidsey and P. C. McIntyre, *Nat. Mater.*, 2011, **10**, 539–544.
11 B. Seger, T. Pedersen, A. B. Laursen, P. C. K. Vesborg, O. Hansen and I. Chorkendorff, *J. Am. Chem. Soc.*, 2013, **135**, 1057–1064.
12 R. E. Brandt, M. Young, H. H. Park, A. Dameron, D. Chua, Y. S. Lee, G. Teeter, R. G. Gordon and T. Buonassisi, *Appl. Phys. Lett.*, 2014, **105**, 263901.
13 S. Hu, M. R. Shaner, J. A. Beardslee, M. Lichterman, B. S. Brunschwig and N. S. Lewis, *Science*, 2014, **344**, 1005.
14 A. Paracchino, N. Mathews, T. Hisatomi, M. Stefik, S. D. Tilley and M. Grätzel, *Energy Environ. Sci.*, 2012, **5**, 8673–8681.
15 A. Paracchino, V. Laporte, K. Sivula, M. Grätzel and E. Thimsen, *Nat. Mater.*, 2011, **10**, 456–461.
16 S. D. Tilley, M. Schreier, J. Azevedo, M. Stefik and M. Graetzel, *Adv. Funct. Mater.*, 2014, **24**, 303–311.
17 C. G. Morales-Guio, S. D. Tilley, H. Vrubel, M. Grätzel and X. Hu, *Nat. Commun.*, 2014, **5**, 3059.
18 J. Luo, L. Steier, M.-K. Son, M. Schreier, M. T. Mayer and M. Grätzel, *Nano Lett.*, 2016, **16**, 1848–1857.
19 P. Dai, W. Li, J. Xie, Y. He, J. Thorne, G. McMahon, J. Zhan and D. Wang, *Angew. Chem.*, 2014, **53**, 13493–13497.
20 W. Cui, W. Niu, R. Wick-Joliat, T. Moehl and S. D. Tilley, *Chem. Sci.*, 2018, **9**, 6062–6067.
21 L. Pan, J. H. Kim, M. T. Mayer, M.-K. Son, A. Ummadisingu, J. S. Lee, A. Hagfeldt, J. Luo and M. Grätzel, *Nat. Catal.*, 2018, **1**, 412–420.
22 C. Li, T. Hisatomi, O. Watanabe, M. Nakabayashi, N. Shibata, K. Domen and J. J. Delaunay, *Energy Environ. Sci.*, 2015, **8**, 1493–1500.
23 W. Niu, T. Moehl, W. Cui, R. Wick-Joliat, L. Zhu and S. D. Tilley, *Adv. Energy Mater.*, 2018, **8**, 1702323.
24 W. Septina, R. R. Prabhakar, R. Wick, T. Moehl and S. D. Tilley, *Chem. Mater.*, 2017, **29**, 1735–1743.
25 V. Duzhko, V. Y. Timoshenko, F. Koch and T. Dittrich, *Phys. Rev. B*, 2001, **64**, 075204.
26 T. Dittrich and S. Fengler, *Surface Photovoltage Analysis of Photoactive Materials*, 2020.
27 Y. H. Choi, K. D. Yang, D.-H. Kim, K. T. Nam and S. H. Hong, *Mater. Lett.*, 2017, **188**, 192–196.
28 J. Lee, H. Yoon, S. Kim, S. Seo, J. Song, B. U. Choi, S. Y. Choi, H. Park, S. Ryu, J. Oh and S. Lee, *Chem. Commun.*, 2019, **55**, 12447–12450.
29 G. Sharma, Z. Zhao, P. Sarker, B. A. Nail, J. Wang, M. N. Huda and F. E. Osterloh, *J. Mater. Chem. A*, 2016, **4**, 2936–2942.
30 A. Song, A. Chemseddine, I. Y. Ahmet, P. Bogdanoff, D. Friedrich, F. F. Abdi, S. P. Berglund and R. van de Krol, *Chem. Mater.*, 2020, **32**, 2408–2419.
31 R. Gottesman, A. Song, I. Levine, M. Krause, A. T. M. N. Islam, D. Abou Ras, T. Dittrich, R. van de Krol and A. Chemseddine, *Adv. Funct. Mater.*, 2020, 1910832.
32 F. F. Abdi, L. Han, A. H. M. Smets, M. Zeman, B. Dam and R. van de Krol, *Nat. Commun.*, 2013, **4**, 2195.
33 M. Butler and D. Ginley, *J. Electrochem. Soc.*, 1978, **125**, 228–232.
34 A. Orendorz, J. Wüsten, C. Ziegler and H. Gnaser, *Appl. Surf. Sci.*, 2005, **252**, 85–88.
35 J. M. Bolts and M. S. Wrighton, *J. Phys. Chem.*, 1976, **80**, 2641–2645.
36 M. Mohamed, K. Irmscher, C. Janowitz, Z. Galazka, R. Manzke and R. Fornari, *Appl. Phys. Lett.*, 2012, **101**, 132106.
37 J. Resasco, H. Zhang, N. Kornienko, N. Becknell, H. Lee, J. Guo, A. L. Briseno and P. Yang, *ACS Cent. Sci.*, 2016, **2**, 80–88.

38 K. H. Ye, H. Li, D. Huang, S. Xiao, W. Qiu, M. Li, Y. Hu, W. Mai, H. Ji and S. Yang, *Nat. Commun.*, 2019, **10**, 3687.
39 V. Stevanović, S. Lany, D. S. Ginley, W. Tumas and A. Zunger, *Phys. Chem. Chem. Phys.*, 2014, **16**, 3706–3714.
40 T. Feurer, P. Reinhard, E. Avancini, B. Bissig, J. Löckinger, P. Fuchs, R. Carron, T. P. Weiss, J. Perrenoud, S. Stutterheim, S. Buecheler and A. N. Tiwari, *Prog. Photovoltaics*, 2017, **25**, 645–667.
41 J. Morasch, H. F. Wardenga, W. Jaegermann and A. Klein, *Phys. Status Solidi A*, 2016, **213**, 1615–1624.
42 P. Prajongtat and T. Dittrich, *J. Phys. Chem. C*, 2015, **119**, 9926–9933.

Open Access Article. Published on 14 September 2020. Downloaded on 10/24/2025 5:08:13 AM.
This article is licensed under a Creative Commons Attribution 3.0 Unported Licence.

 This journal is © The Royal Society of Chemistry 2020